

# PDANet: Pyramid Density-aware Attention Net for Accurate Crowd Counting

Saeed Amirgholipour, *Member, UTS* Xiangjian He, *Senior Member, UTS* Wenjing Jia, *Member, UTS* Dadong Wang, *Senior Member, CSIRO* and Lei Liu, *Member, Beihang University*

**Abstract**—Crowd counting, *i.e.*, estimating the number of people in a crowded area, has attracted much interest in the research community. Although many attempts have been reported, crowd counting remains an open real-world problem due to the vast scale variations in crowd density within the interested area, and severe occlusion among the crowd. In this paper, we propose a novel Pyramid Density-Aware Attention-based network, abbreviated as PDANet, that leverages the attention, pyramid scale feature and two branch decoder modules for density-aware crowd counting. The PDANet utilizes these modules to extract different scale features, focus on the relevant information, and suppress the misleading ones. We also address the variation of crowdedness levels among different images with an exclusive Density-Aware Decoder (DAD). For this purpose, a classifier evaluates the density level of the input features and then passes them to the corresponding high and low crowded DAD modules. Finally, we generate an overall density map by considering the summation of low and high crowded density maps as spatial attention. Meanwhile, we employ two losses to create a precise density map for the input scene. Extensive evaluations conducted on the challenging benchmark datasets well demonstrate the superior performance of the proposed PDANet in terms of the accuracy of counting and generated density maps over the well-known state of the arts.

**Index Terms**—Crowd counting, density aware, attention model,CNN.

## 1 INTRODUCTION

Nowadays, crowd counting has become an important task for a variety of applications, such as traffic control [1], public safety, and scene understanding [2], [3]. As a result, density estimation techniques have become a research trend for various counting tasks. These techniques utilize trained regressors to estimate people density for each area so that the summation of the resultant density functions can yield the final count of crowd.

A variety of regressors, such as Gaussian Processes [4], Random Forests [5], and more recently, deep learning based networks [6], [7], [8] have been used for crowd counting and density estimation. However, the state-of-the-art approaches are mostly deep learning based approaches due to their capabilities of generating accurate density maps and producing precise crowd counting [1], [9].

Generally, deep neural networks (DNNs) based approaches utilize standard convolutions and dilated convolutions at the heart of the models to learn local patterns and density maps [8], [10]. Most of them use the same filters, pooling matrices, and settings across the whole image, and implicitly assume the same congestion level everywhere [6]. However, this assumption often does not hold in reality.

To better understand the effect of this mis-assumption, let us show some examples with clearly different levels

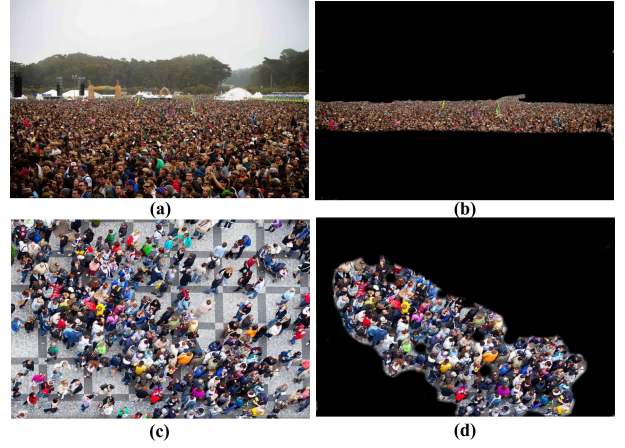


Fig. 1. Examples of crowded and sparse images. (a) and (c) show an example of a highly crowded scene and a less crowded scene, respectively, while (b) and (d) show their corresponding congested areas.

of crowdedness. Fig. 1 presents some exemplar images of different congestion scenarios. Fig. 1(a) shows a highly crowded image having more than 1,000 people, while Fig. 1(c) presents a less crowded scene having less than 70 people. However, if we look at Fig. 1(a), we notice that there is a relatively more congested area, which is shown in Fig. 1(b). The same situation can be seen in Fig. 1(c), and it is obvious that a small area within this crowd, as shown in Fig. 1(d), is more crowded.

Due to this dynamic variation in the crowded scenes, naturally we should utilize different features and branches to respond and capture details at different levels of crowdedness. In the past, this has been attempted by four ma-

• Saeed Amirgholipour, Xiangjian He, and Wenjing Jia are with the School of Electrical and Data Engineering, University of Technology Sydney, Australia. email:;  
E-mail: Saeed.AmirgholipourKasmani@student.uts.edu.au; Xiangjian.He@uts.edu.au; Wenjing.Jia@uts.edu.au

• Dadong Wang is with the Quantitative Imaging, CSIRO Data61, Australia E-mail: Dadong.Wang@csiro.data61.au

• Lei Liu was in School of Instrumentation Science and Opto-Electronics Engineering, Beihang University, China. E-mail:by1417114@buaa.edu.cn

ajor types of approaches, *i.e.*, defining separate pathways from the lower layers and utilizing different sizes of the convolutional filters, image pyramid-based methods [1], [11], detection-based crowd counting [6], patch-based crowd counting [10], [12], [13], and multi-level feature based methods [11]. Although these methods have achieved robust performance with some different tactics, there are still lots of spaces to improve their performances by designing highly efficient convolutional layer structures, which can effectively deal with crowd scenes with dramatic density varieties effectively.

First, generally speaking, a kernel size of  $3 \times 3$  for a convolution filter is more effective than the larger ones in terms of extracting more meaningful features, because more details can be captured with lower complexities without making it more difficult to train the network [14], [15], [16]. Kang *et al.* [17] proved that smaller receptive fields gave better performance. Secondly, using patch-based processing and multi-patch processing is time costly due to that the same features have to pass through different paths and patches multiple times. If we want to take benefit of the multi-patch or multi-column based approaches, it is better to extract some coarse features from the initial layers and then pass them to some branches for further zooming in to find more sophisticated features. To utilize a deeper network for crowd counting, we need an approach that can deploy the aforementioned proposals on the multi-column structure to achieve better performance.

In this paper, we present a deep encoder-decoder based architecture named as Pyramid Density-aware Attention-based Network (PDANet), which combines the pyramid feature extraction with spatial and channel attentions to produce richer features estimating crowd of various levels of crowdedness and scales. In our work, we use the VGG16 as the feature extractor for the encoder to produce features for the decoder of the model. To learn multi-scale features, we first use a cascade of global average pooling (GAP),  $1 \times 1$  convolution and dilated convolutions with kernels of  $3 \times 3$  to extract more mature features with different scales from VGG16 features. Then, we apply the channel and spatial attentions in different layers to enhance and boost the quality of features in order to obtain more accurate density maps. On the other hand, to make the model adaptive to different density levels within an image, we introduce a classification module to classify the crowdedness level of the input scene and develop generation models of low and high crowded density maps.

This work is different from the existing crowd counting approaches that use the pyramid contextual information and attention modules in several ways.

(a) The first main characteristic of our proposed PDANet is its density awareness by adopting the pyramid and attention modules. Different from other works attempting to address this problem of density variety, *e.g.* [12], our PDANet does not separate the input scene into different patches. Instead, we use multipath branching to address the intra-density variations within the input scene. Experimental results have shown that, the pyramid and attention modules have contributed a 5 to 20 percent improvement over the baseline model.

(b) Pyramid Feature Extractor (PFE) is the second no-

ticeable contribution of our PDANet. We utilize a new combination of global average pooling,  $1 \times 1$  convolution, and Atrous convolution, which is different from the existing approaches in terms of the orders and parameters that can better aggregate local scale features and is more effective than the existing solutions.

(c) The third remarkable feature of PDANet is its attention modules. The architecture of our end-to-end attention modules is also different from ADCrowdNet [18] because it uses the combination of the spatial and channel based attention modules within the architecture. Furthermore, it is trained in an end-to-end way based on the crowd counting dataset, instead of separately as in ADCrowdNet [18]. Compared with the work in [19], our PDANet has also adopted another spatial-based module in the DAD module to optimize the density map results based on feature maps of the sparse and dense area within the input scene.

(d) The last distinct characteristic of the PDANet is classification modules, which are different from the existing work [19]. Our PDANet passes the input image to two different sub-models with different receptive fields to evaluate lower and higher bound of the density map, and then combines them with the help of channel attention module. Our PDANet introduces a classification module that classifies the input image to the low or high-density data and passes them to the appropriate corresponding DAD module.

To summarize, the contributions made in this paper are as follows.

- In order to address crowd areas of various scales and density levels, we propose a density-aware solution, which is achieved with the combination of multi-scale feature extraction, density classification and adaptive density estimation modules. This feature helps the model to handle density variation between different images as well as within each input scene.
- We first integrate the pyramid multi-scale feature extraction mechanism in feature extractor to extract rich features for the following classification module. Then we integrate the channel and spatial attention modules and propose an end-to-end trainable density estimation pipeline. Both modules have contributed to exploit the right context at each location within a scene.
- For estimating densities of crowd with not only high and low crowdedness levels but also inter-level density areas, we propose to use a combination of classification and regression losses to address the whole and within-the-scene changes in the density maps.

Extensive experiments on several challenging benchmark data sets are conducted to demonstrate the superior performance of our proposed PDANet approach over the state-of-the-art solutions. We also preform comprehensive ablation studies to validate the effectiveness of each component in our proposed approach.

## 2 RELATED WORKS

In this section, we provide literature review related to our PDANet model.

Although early solutions to crowd counting focused on counting by detection. Unfortunately, due to their incapability of handling highly congested scenes [10], they fail to deal with those more challenging, very crowded scenes. In recent years, counting by regression has become the most popular crowd counting approach, which learns a regressor that depicts the relationship between image characteristics and the density or object count [1], [6], [12], [19]. Thus, regression models based on the deep neural networks (DNNs) have become the dominant ones for density estimation and crowd counting.

Due to the excellent ability of CNN to learn local patterns, researchers have started to utilize it for regressing the density map and crowd counting [11], [20], [21]. In the earlier researches about crowd counting, researchers focused on using a single branch or scale crowd counting [5], [22]. With the CNN-based models, they superseded the previous studies that utilized the traditional models such as Gaussian Process or Random Forests as a regressor [4]. One of the best single column methods was proposed by Li *et al.* [20], and it combined VGG-16 [14] and dilated convolution layers to handle multi-scale contextual information.

However, there still exists a significant issue that is the huge variation of people sizes among different datasets and within an input scene [23]. To deal with this, some researchers tried to utilize the patch-based processing [10], [24]. They divided the scenes into some overlapping patches and then fed them to the CNN-based models to estimate the final density map [24]. Although these approaches were able to improve the accuracy significantly, they had a big drawback, *i.e.*, high time cost. Therefore, researchers came up with a new idea, *i.e.*, to utilize multi-scale networks to do the density estimation task [1], [21]. Cao *et al.* [21] introduced a CNN-based SANet, where the encoder extracted the scale diversity in its features by using an aggregation module and the decoder utilized transposed convolutions to generate high-resolution density maps. Experimental results demonstrated that their model could achieve superior performance to the-state-of-the-art methods.

Many studies have been done based on multi-column architectures [12], [25]. One of the initial works was done by Zhang *et al.* [25], who proposed a three-CNN-column based MCNN structure, each with different receptive parameters to handle a range of different head sizes. MCNN has improved the-state-of-the-art results remarkably. Based on the idea of MCNN, a multi-column patch-based model, Switch-CNN [12], [25] was proposed by Sam *et al.*. Their approach used the concept of patch classification and multi-scale regressors for generating the density map. IG-CNN [26] was another extensive study that combined the clustering and crowd counting for estimating the density map more adaptively based on training a mixture of experts that could incrementally adapt and grow based on the complexity of the dataset. Sindagi *et al.* proposed a new multi-column network, *i.e.*, CP-CNN [27], which added two other branches to classify an image-wise density to provide the global and local context information to the MCNN model. Recently, Deb *et al.* [28] incorporated the Atrous convolutions into the multi-branch network by assigning different dilation rates to various branches.

Most recently, Kang *et al.* [17] proposed a model that

used image pyramids to handle multiple scales within the scenes. They created an image pyramid of the input scene and passed each image through the FCN to get the output density maps, and then fused them adaptively at every pixel location. Shi *et al.* [29] proposed a perspective information CNN-based model PACNN for crowd counting. Their model combined the perspective information with density regression to address the person scale change within an image. They generated the ground truth perspective maps and used it for generating perspective-aware weighting layers to combine the results of multi-scale density adaptively. Wan *et al.* [30] proposed a new model RRSP to utilize the correlation information among training dataset (residual information) for accurate crowd counting. They fused all the residual predictions and created the final density map based on the appearance-based map and the combined residual maps from the input scene.

Recent studies mostly focused on utilizing the pyramid and attention-based modules [31]. Pyramid modules were introduced by Zhao *et al.* [32] to produce proper quality features on the scene semantic segmentation task. They introduced an efficient method to estimate the head size and combined it an attention module to aggregate density maps from different layers and generate the final density map. Liu *et al.* [1] presented another end-to-end multi-scaled solution CAN based on fusing multi-scale pyramid features. They used modified PSP modules for extracting multi-scale features from the VGG16 features to address the rapid scale change within the scenes. Their model leveraged multi-scale adaptive pooling operations to cover a variety range of receptive fields. Compared to CAN, Chen *et al.* proposed an end-to-end single-column structure as a Scale Pyramid Network (SPN), which extracted multi-scale features with the dilated convolution with various dilation rate (2, 4, 8, and 12) from the VGG16 backbone features [11]. The experimental results proved that their idea worked well on some well-known datasets.

On the other hand, the attention module and idea proposed by [33] aimed to re-calibrate the features adaptively, so as to highlight the effect of valuable features, while suppressing the impact of weak ones [34]. Recently, researchers attempted to incorporate this module and its variations into their models to improve the performance in several tasks such as object detection, object classification, and medical image processing [35], [36], [37]. Rahul *et al.* proposed an attention-based model to regress multi-scale density maps from several intermediate layers [18]. ADCrowdNet [18] was one of the latest research in the area of crowd counting, and it used attention modules to generate accurate density maps. Liu *et al.* utilized a two-step cascade encoder-decoder architecture, one for the detection of the crowded areas and producing the attention map (AM), and the other for generating density maps (DME). Their method achieved excellent results on the ShanghaiTech Part A dataset. Although the idea of using the attention map was interesting, it has some significant drawbacks, such as that (a) it needed an external dataset to train AMG to detect the crowd area, and (b) after producing the attention map it will apply on the input crowd image to create a masked input data for DME, which is redundant and time consuming. Wu *et al.* [19] proposed an adaptive multi-pass model ASD for crowd counting. Their

model had three branches, two for sparse and dense crowd counting with different respective fields, and the third layer for adaptively recalibrating the effect of each density map to produce the final density output.

### 3 PYRAMID DENSITY-AWARE ATTENTION NET

In this section, we first present the general structure of our proposed PDANet for adaptively addressing the challenges in crowd counting. This new structure uses pyramid-scale feature extraction and consists of adaptive pooling, and  $1 \times 1$  and  $3 \times 3$  convolutions to enrich the feature maps for handling objects of various scales within a scene. In the following subsections, we will give more details about the attention modules, pyramid feature modules, decoders and loss functions.

#### 3.1 Overview

As discussed above, we formulate crowd counting as the problem of regressing people’s density map from a scene. The overall architecture of our PDANet for regressing the density map of the crowd from an image is illustrated in Fig. 2.

This framework contains five main components, *i.e.*, a Feature Extractor, a Pyramid Feature Extractor (PFE), a Classifier, a Density Aware Decoder (DAD), and an Attention Module. Each of these components contributes to the overall accuracy and efficiency of the model for crowd counting.

The backbone of our PDANet is a network based on VGG16 [14], which is widely used for extracting low-level features. We eliminate layers between the last two pooling layers considering the trade-off between resource cost and accuracy [20]. Then, we apply a channel and spatial based attention module to it to highlight essential features. Then, these features are fed into the PFE module, which incorporates the combination of adaptive pooling and  $1 \times 1$  and  $3 \times 3$  dilated convolution to produce scale-aware mature features for last layers of the decoder module. In the next step, we incorporate a Global Average Pooling (GAP) and a fully connected layer to classify the input scene as a high-density or a sparse one. Then, we pass this information to the respective decoder with the same structure (our theoretical studies proved that the same respective field is better than a different one). The decoders contain four  $3 \times 3$  dilated convolution layers, which are empowered with an attention module after each layer.

Furthermore, to address the congestion difference within dense or sparse areas, we design two branches of the decoder module to generate low and high-density maps within the input scene and assign them to the corresponding regression losses. In the final step, we use the dense and sparse features from the last layer of the decoders to produce the final output density map (DM). Our PDANet uses the same loss for sparse, dense and final output DM, and a classification loss to train the model in an end-to-end manner.

To summarize, in our proposed PDANet, each part plays a role in the overall performance:

- The Attention Module focus its attention on the significant features (crowded areas).

- The Pyramid Feature Extractor generates more productive features, which are more suitable for the crowd counting task with scale variation, through a combination of adaptive pooling and dilated convolution with different scales.
- The Classifier helps find the proper branch of the decoder according to the crowdedness level of the area.
- The mid-branch Decoder is to address congestion change within the input image.

#### 3.2 Channel and Spatial based Attention Modules

The Attention block was firstly introduced as a squeeze and excitation (SE) block in [33], which could be easily integrated within the CNN architecture. It utilized the global average pooling to figure out the spatial dependency and made a channel-specific descriptor to emphasize the useful channels and re-calibrate the feature map. Based on this foundation, concurrent spatial and channel squeeze and excitation was proposed to apply channel and spatial based re-calibration concurrently [34].

In this study, we re-calibrate the feature maps adaptively by mixing attention modules to augment the effect of essential features, while suppressing the weak ones. We use the combination of spatial and channel-based attention for finding and separating the crowded area within the input image. As it is shown in Fig. 2, we utilize an attention module in our model, which is the channel and spatial attention [34] after the convolution layers, shown as the green module in Fig. 2. This module contains channel and spatial attention to produce the final attention features in each layer. We consider the maximum value of each index location between the channel and spatial attention outputs.

The other attention module is a spatial attention map that is generated based on the density map of the sparse and dense crowded areas within the image. We apply a sigmoid on this attention module and multiply it with the joint convolution feature maps from the last layer of a sparse and dense decoder.

Fig. 3 illustrates this attention module. As shown in this figure, there are two branches in this illustration, *i.e.*, the channel attention branch on the top, and the spatial attention branch on the bottom. The channel attention branch utilizes a cascade of Global Average Pooling (GAP) and two fully connected layers with the size of  $\frac{C}{2}$  and  $C$ , respectively ( $C$  is the channel size of a convolution layer). Then, multiplying its results to the input feature maps.

To apply the channel based attention mechanism, we first perform GAP on the input feature map  $F_{in}$ , as  $V$ , and then transform them by two fully-connected layers  $fc_1$  and  $fc_2$ , as shown in Fig. 3 and Eq. 1 as:

$$F_{in}^{cAM} = fc_2(sig(fc_1(V))), \quad (1)$$

where  $sig$  is a sigmoid function that yields the value in a range of  $[0, 1]$  to find the impact of each layer in the feature maps.

Finally, for channel based attention, features  $F_{out}^c$  are obtained by multiplying the encoded channel-wise dependencies ( $F_{in}^{cAM}$ ) to  $F_{in}$  to get  $F_{out}^c$ .

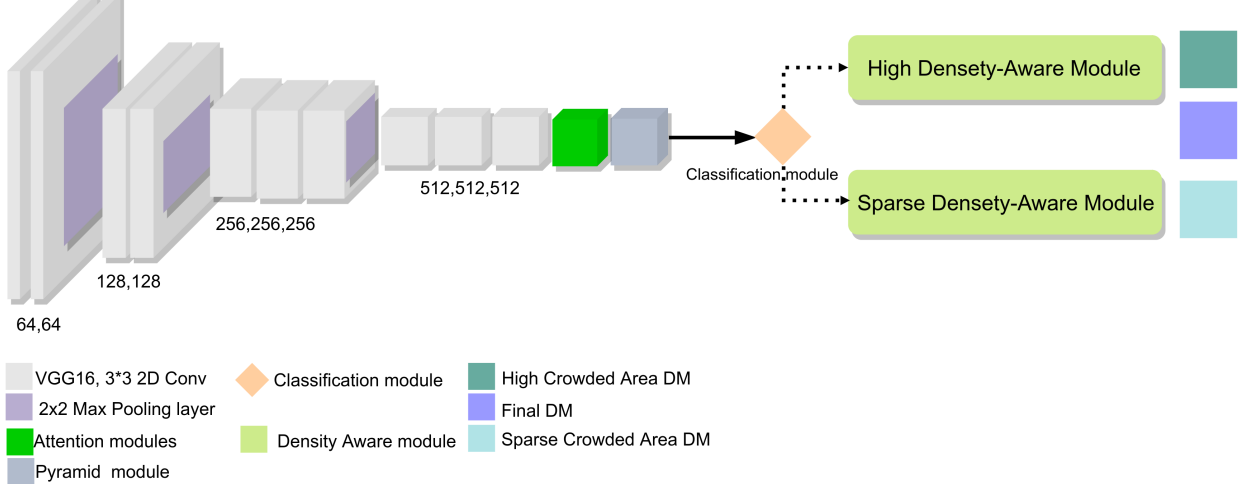


Fig. 2. The overview of our proposed PDANet network. This architecture contains a VGG16 based feature extractor, a Pyramid module, an Attention module, a Classification module, and a Decoder module.

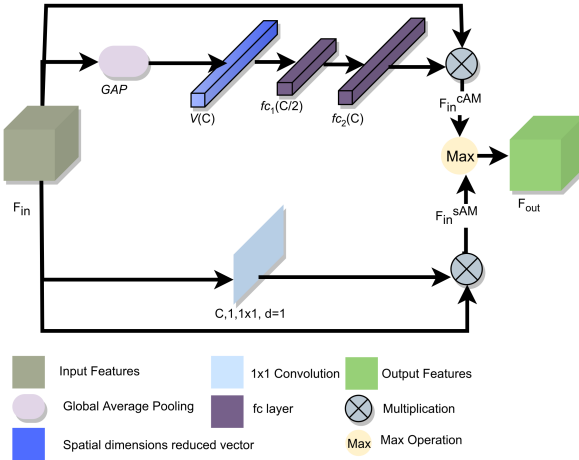


Fig. 3. Illustration of the attention module of our model. The top branch generates channel-based attention, while the bottom branch generates the spatial attention map.

On the other hand, to obtain the spatial attention map,  $F_{in}^{SAM}$ , we perform a  $1 \times 1$  convolution, *i.e.*,  $Conv \in \mathbb{R}^{1 \times 1 \times C \times 1}$ , on the input feature maps. Thus, we can measure the importance of a spatial information  $(i, j)$  of each area within  $F_{in}$ . In the next stage, we multiply the spatial attention map to the input feature maps to get the final spatial attention features  $F_{out}^s$ , which augment relevant spatial locations and suppress irrelevant ones.

Finally, we combine the results of these two attentions by element-wise max of the channel and spatial excitation, *i.e.*,  $F_{out} = \max(F_{out}^c, F_{out}^s)$ . These feature maps amplify the input feature map data and re-calibrate the crowded area within each input convolution layer.

### 3.3 Pyramid Feature Extractor (PFE)

As discussed in Section 1, we need to capture details at various scales of crowd density within the input images to respond to the limitation of the same receptive field. In this section, we propose a Pyramid Feature Extractor (PFE),

which is inspired by the Spatial Pyramid Pooling [11] to address this issue. The PFE fuses features under various pyramid scales by a combination of GAP and two shared 2D convolution layers with a mixture of  $1 \times 1$  and  $3 \times 3$  dilated kernels. The general operation of PFE is illustrated in Fig. 4.

We extract contextual features as:

$$GAP_i = (P_{ave}^i(F_{in})), \quad (2)$$

where, for each scale  $i$ ,  $GAP_i$  calculates the average by performing  $P_{ave}^i$  over the input feature maps and produce  $s(i) \times s(i)$  contextual features for each channel. Various scales of contextual features form the pooled representation for different areas and provide rich information about the density level in various sub-regions of the input image.

In the Ablation study section, we compare several scenarios for GAP. The results presented in the Experiments section are based on the utilizing three GAPs.

Then, we feed  $GAP_i$  to the Conv Module to improve the representation power of the feature map. This procedure is different from the architectures that reduce the dimension with convolution [11].

As illustrated in Fig. 4, we perform the Conv operation as:

$$CF_i = U_{bi}(F_1^i(F_{512 \rightarrow 32}^r(GAP_i)) + F_3^i(F_{512 \rightarrow 32}^r(GAP_i))), \quad (3)$$

where, for each scale  $i$ ,  $CF_i$ , is the shared Conv module that comes with a bi-linear interpolation to up-sample the contextual features to be of the same size as  $F_{in}^P$ . These operations reduce the number of parameters to learn in PFE, speed up the processing, and increase the model efficiency.

On the other hand, with passing input features to the shared layers, we extract local feature patterns invariantly as kernels traveling across all the image positions in different  $GAP_i$  and detect local learned patterns. The shared layer contains one  $1 \times 1$  convolution to reduce the number of channels from 512 to 32. We do this to reduce the number of parameters that need to train and reduce the computational cost of PFE.

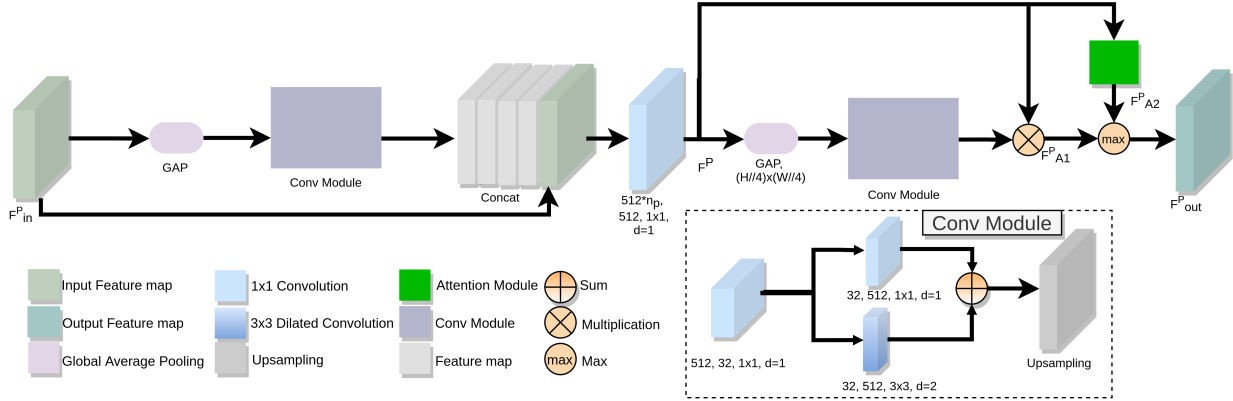


Fig. 4. The overview of the Pyramid Feature Extractor (PFE) module. The PFE module uses  $1 \times 1$  and  $3 \times 3$  dilated kernel convolution with the GAP to extract features of different scales from the VGG16 features.

In the next stage, we get the summation of a  $1 \times 1$  convolution, and a  $3 \times 3$  dilated convolution as a piece of extra bonus information about the contextual features  $GAP_i$ . Experimentally, we verify that this combination of convolution filters improves the performance of the PFE module in the density estimation task.

Finally, we concatenate all  $CF_i$  and the input features  $F^P_{in}$  with a  $1 \times 1$  convolution. We reduce the number of the channels to the original VGG features  $F^P_{in}$ . We define this as:

$$F^P = F_{n_p \times 512 \rightarrow 512}^r(Concat(CF_i, F^P_{in})), \quad (4)$$

where  $n_p$  is the number of pyramid contextual features  $CF_i$ , plus the original input feature map.

Then, we utilize a special attention module, which is the combination of the Conv module and attention module that we explained in Section 3.2. We pass  $F^P$  to two separate attention branches. As illustrated in Fig. 4, in the bottom, we feed the  $F^P$  to the GAP with the size  $i = F_{size}/4$ , and then apply the Conv module on it. We apply the GAP with the size  $i = F_{size}/4$  to highlight and escalate the most important parts of the output feature maps. Then, we apply the element-wise multiplication to produce the Conv module feature map output ( $F^P_{A1}$ ). On the top, we also perform the attention module that we discussed in the session 3.2 to generate the attention feature map output ( $F^P_{A2}$ ). Finally, we combine the results of these two attentions by element-wise *max* operation of the Conv module output ( $F^P_{A1}$ ) and the attention module output ( $F^P_{A2}$ ), which is defined by:

$$F^P_{out} = \max(F^P_{A1}, F^P_{A2}), \quad (5)$$

Altogether, as illustrated in Fig. 4, the PFE module extracts contextual features  $CF_i$  as discussed above, which are then fed to the classification module and a Density Aware Decoder (DAD) module that produces the density map.

### 3.4 Classification Module

The next step in our overall framework, as illustrated in Fig. 2, is to decide whether the input contextual features are dense or sparse. We do this to address the huge variation of crowd densities among different images. We pass input features to the suitable DAD to adaptively react to the density level of the input image and provide better estimation for crowd density.

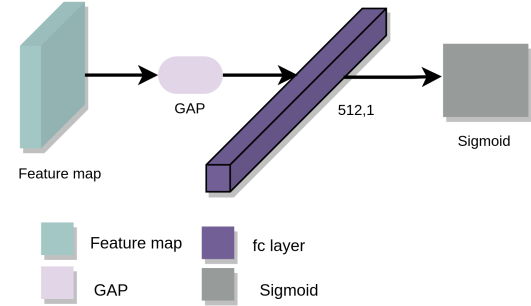


Fig. 5. Illustration of the classification module of PDANet. It uses the global average pooling with fully connected layer to determine the dense level of input scene.

To model this, as it is shown in Fig. 5, we introduce a binary classification module to learn to classify the input feature maps into two classes, *i.e.*, dense or non-dense (*aka*, sparse), as:

$$O_c = \text{sig}(fc(GAP_{1,1})), \quad (6)$$

where  $GAP_{1,1}$  is global average pooling with the scale of  $1 \times 1$ , which produces a vector with the size of 512,  $fc$  is a fully connected layer, and  $\text{sig}$  is a sigmoid function that yields the value in a range of  $0 \rightarrow 1$  to find the impact of each layer in the feature maps.

Thus, the classification module produces a class probability which is a value in the range of  $0 \rightarrow 1$ . If the output probability ( $O_c$ ) is less than 0.5, the model considers the input as a non-dense crowd image and passes it to the sparse DAD branch; otherwise it passes it to the high DAD branch, as shown in Fig. 2.

### 3.5 Density Aware Decoder (DAD)

DAD is one of the special modules of our proposed PDANet model, as it dynamically handles intra-variation of the density level within the input image. To achieve this, we use four dilated convolution layers with the attention module attached to each layer, similar to the one introduced in Section 3.2. Through classifying feature maps and passing the high density areas to the high DAD branch, and low density areas to the sparse branch, we achieve a model that is able to address the density variation of the input

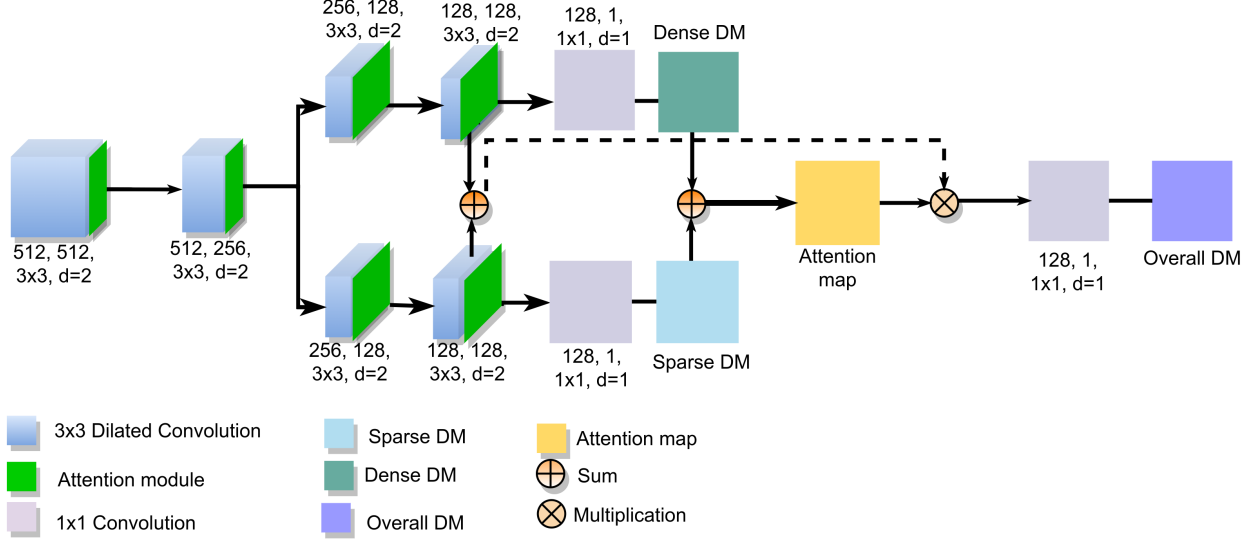


Fig. 6. The illustration of the DAD module. The input feature maps are fed to the two shared layers and then we use the two branches to handle the dense and sparse areas within the scene.

image adaptively. Furthermore, the DAD is composed of two parts, *i.e.*, the shared layers and the low or high-density decoder branches. This design enables us to cope with various occlusion, internal change, and diversified crowd distribution, as illustrated in Fig. 1.

The structure of DAD is illustrated in Fig. 6. As shown in the figure, we consider the first two layers as shared layers and then pass the output feature maps to two separate paths with the other two convolution layers to manage the within-image density variation. The number of channels in the dilated convolution in DAD is ( $N_{ch} = 512, 256, 128, 128$ ) with the kernel filter size  $3 \times 3$  and the dilation rate  $d_{rate} = 2$ . Furthermore, to reduce the number of training parameters, we utilize a  $1 \times 1$  convolution to reduce the input channels to 32 and then perform 2D dilated convolution on the reduced channel feature maps. This processing speeds up the training and convergence of our model. In each branch, we have a  $1 \times 1$  convolution at the end to produce the density maps for the low and dense crowded areas. We call these layers as  $CM_d$  and  $CM_s$ , respectively.

Moreover, there is a small notation. For the highly dense and low dense image areas, we use the  $CM_d$  for the high dense regions within the image. However, for the low density regions, within the low or high dense input image, we have used a shared  $CM_s$  layer. This design gives us the benefit of using more information to train the model to map the low and dense regions with the input image. Therefore, we are able to have a better density estimation for the low crowded areas. On the other hand, by utilizing a different  $CM_d$  for the highly-dense areas within the input image, our DAD module is able to improve its estimation for these areas too.

By utilizing this architecture in the DAD, we will have two resultant density maps for the low and high crowded areas of the input image. Besides this, we pick up the feature map of the last layer in the dense and non-dense branch. Then, we sum up these feature maps and name the sum as  $F_s$  and utilize the summation of low and high-density maps

as an attention module  $A_s$ . Therefore, we use the following equation to produce the final overall feature map:

$$F_f = F_s \times \text{sig}(A_s), \quad (7)$$

where  $\text{sig}(A_s)$  is the sigmoid scaling of the  $A_s$ , and  $F_f$  is the final overall feature map, which is fed to the final layer to produce an overall dense map. This novel design enables DAD to handle various occlusion, inter and intra crowd density variation.

### 3.6 Implementation Details

The last part of PDANet is about the loss function. The PDANet uses two significant losses, which fall into two categories, *i.e.*, the regression and the classification losses. We explain them in details in the following sections.

#### 3.6.1 Regression Loss and Ground Truth

For the regression loss, we utilize a combination of three different error measurements, *i.e.*, counting error  $\ell^c$ , various scale error  $\ell^2$ , and escalated error  $\ell^{es}$ , respectively. We measure the counting error  $\ell^c$  as an absolute difference between ground-truth and the estimated crowd count, with the following equation:

$$\ell^c = \left| \sum_{i=1}^N D_i^{gt} - \sum_{i=1}^N D_i^{est} \right|, \quad (8)$$

where  $N$  is the number of pixels in an input scene,  $D_i^{gt}$  and  $D_i^{est}$  are the ground-truth and the estimated crowd count at location  $i$  for  $i = 1, 2, \dots, N$ , respectively.

We rely on the same methodology as that in the previous work to obtain the ground-truth density map  $D_i^{gt}$  [21], which is generated by convolving each delta function  $\delta(x - x_i)$  with a normalized Gaussian kernel  $G_\sigma$  [21] as:

$$D_i^{gt} = \sum_{x \in S_I} \delta(x - x_i) \times G_\sigma(x), \quad (9)$$

where  $S_I$  represents the number of annotated points in the image  $I$ , and  $x_i$  is the  $i$ -th annotated point.

Note that the summation of the density map ( $D_i^{gt}$ ) is equal to the crowd count in the image. Instead of using the geometry-adaptive kernels [20] in Eq.9, we use a fixed spread parameter  $\sigma$  of the Gaussian kernel for generating ground truth density maps.

For the proposed PDANet, we need to separate sparse and dense regions within the input scene to extract the dense and sparse regression losses for each input image. To obtain  $D_{d,i}^{gt}$  or  $D_{s,i}^{gt}$  representing the density map at location  $i$  falling into a dense or sparse region in the input image, we utilize a simple rule, which is defined by:

$$D_{d,i}^{gt} = \begin{cases} D_i^{gt}, & \text{if } D_i^{gt} > \text{mean}\{D_i^{gt}, i = 1, 2, \dots, N\}, \\ 0, & \text{else,} \end{cases} \quad (10)$$

$$D_{s,i}^{gt} = \begin{cases} D_i^{gt}, & \text{if } D_i^{gt} \leq \text{mean}\{D_i^{gt}, i = 1, 2, \dots, N\}, \\ 0, & \text{else,} \end{cases} \quad (11)$$

The various scale error  $\ell^2$  measures the pixel-wise errors of various scales. To obtain this error, we again utilize the Global Average Pooling (GAP) on the ground truth and the estimated density map. We apply three scales of GAP, i.e., dividing each of the target and input density maps with divisors of 2, 4 and 8, respectively. For example, for the input density map with size of  $H \times W$ , we apply GAP with divisor of 2 to generate the corresponding GAPs' density maps with the size of  $\frac{H}{2} \times \frac{W}{2}$ . Then, we measure the  $\ell^2$  for each scale by:

$$\ell^2 = \sum_{i=1}^N \left| D_i^{gt} - D_i^{est} \right|^2, \quad (12)$$

where  $D_i^{gt}$  and  $D_i^{est}$  are the ground-truth and the estimated density maps for each of the three different scales, respectively. We denote these three scale errors  $\ell_{s2}^2$ ,  $\ell_{s4}^2$  and  $\ell_{s8}^2$ , respectively. These errors help us to accurately handle the density variation in each scale of the input scene.

The escalated error mostly focuses on addressing the area with a high difference between the ground truth and the estimated density map. To extract this error, we need to extract the absolute difference between the estimated density map and its ground truth density at each location  $i$  as shown in Eq. 13 below, where  $i = 1, 2, \dots, N$ . is defined by:

$$\ell_i^1 = \left| D_i^{gt} - D_i^{est} \right|, \quad (13)$$

Then, we calculate the average difference  $\ell^1$  from  $\ell_i^1$ ,  $i = 1, 2, \dots, N$  by:

$$\ell^1 = \frac{\sum_{i=1}^N \ell_i^1}{N}, \quad (14)$$

Then, we use  $\ell^1$  to add extra weight to the area with higher misestimated value. We also force PDANet to generate escalated errors values for a region with no people or objects. It is done by augmenting the corresponding  $\ell_i^1$  values by 10 times. The escalated difference error  $\ell_i^{es}$  at

location  $i$ , for  $i = 1, 2, \dots, N$ , and the overall escalated error  $\ell^{es}$  are defined by:

$$\ell_i^{es} = \begin{cases} 10 \times \ell_i^1, & \text{if } \ell_i^1 \leq \ell^1, \\ 10 \times \ell_i^1, & \text{else if } D_i^{gt} == 0, \\ \ell_i^1, & \text{else,} \end{cases} \quad (15)$$

and,

$$\ell^{es} = \sum_{i=1}^N \ell_i^{es}, \quad (16)$$

Then, the overall regression loss, denoted by  $\ell_o^{reg}$ , is defined by:

$$\ell_o^{reg} = \ell^{es} + \ell^c + \ell_{s2}^2 + \ell_{s4}^2 + \ell_{s8}^2, \quad (17)$$

When  $D_i^{gt}$  in Eqs. 8, 12, and 13, is replaced by  $D_{d,i}^{gt}$  and  $D_{s,i}^{gt}$  respectively, then the results from Eq. 17 define the dense regression loss and the sparse regression, which are denoted by  $\ell_d^{reg}$  and  $\ell_s^{reg}$ , respectively.

### 3.6.2 Classification Loss and Ground Truth

On the other hand, according to our model, we need to classify the scene. Thus, we introduce  $Cl_t^{gt}$  as an actual class tag. To obtain the  $Cl_t^{gt}$ , we define a rule to decide whether the input image is highly crowded or not.

We consider  $Dl_p$  as a measure of dense level of the input scene, which is defined by:

$$Dl_p = \frac{\sum_{i=1}^N D_i^{gt}}{(D_i^{gt} > 0) \cdot \text{sum}}, \quad (18)$$

where  $(D_i^{gt} > 0) \cdot \text{sum}$  counts the number of pixels that have a positive density value.

Then, according to the change in the number of people in each dataset, we can find a threshold  $\tau$ . Thus, we define a  $Cl_t^{gt}$  by:

$$Cl_t = \begin{cases} 1, & \text{if } Dl_p > \tau, \\ 0, & \text{else,} \end{cases} \quad (19)$$

If the dense level of the input scene  $Dl_p$  is larger than that the threshold  $\tau$ , we consider it as a high density input scene; otherwise, it is a low density one. We have tested different threshold values  $\tau$ , and found that our model is not too sensitive to it and able to classify the input scenes correctly.

Then, we consider the Binary Cross Entropy (BCE) loss to train the model to detect sparse and dense input images, where  $\text{BCE}(Cl_t^{gt}, Cl_t^{est})$  is defined by:

$$\text{BCE}_{loss} = - \left[ Cl_t^{est} \cdot \log Cl_t^{gt} + (1 - Cl_t^{est}) \cdot \log(1 - Cl_t^{gt}) \right], \quad (20)$$

where  $Cl_t^{gt}$  and  $Cl_t^{est}$  are the actual class and the class predicted by the model, correspondingly.

### 3.6.3 Total Loss

Finally, by helping with these losses, we need to define a rule to train the model efficiently. As it is obvious from the structure of the model, we need to detect and correctly pass high and sparse dense input to the corresponding DAD. Therefore, we need to penalize the model whenever

it cannot detect the dense level of the input scene. Thus, we use the following equation to combine different losses:

$$Sum_{loss} = \ell_o^{reg} + \alpha \times (\ell_d^{reg} + \ell_s^{reg}), \quad (21)$$

and

$$Final_{loss} = BCE_{loss} \times \ell_o^2 + Sum_{loss}, \quad (22)$$

where  $\alpha$  sets to 0.4 according to empirical studies.

According to the  $Final_{loss}$ , by adding the  $BCE_{loss} \times \ell_o^2$ , we are able to overcome the mis-classification of the input scene. With  $Sum_{loss}$ , the model can learn the dense and sparse area within an input image precisely.

## 4 EXPERIMENTS

In this section, we evaluate the performance of our proposed approach. We first introduce the evaluation metrics and then report experimental results obtained on benchmark datasets. The experiments are conducted on four benchmark datasets and results are compared with the recently published state-of-the-art approaches, which have already been used for comparison purpose since. We then perform a detailed ablation study.

### 4.1 Evaluation Metrics

Previous works on crowd density estimation have used the Mean Absolute Error (MAE) and the Root Mean Squared Error (MSE) as evaluation metrics [1], [11], [20], [21], which are defined by:

$$MAE = \frac{1}{M} \sum_{i=1}^M |C_i^{est} - C_i^{gt}|, \quad (23)$$

and

$$MSE = \sqrt{\frac{1}{M} \sum_{i=1}^M (C_i^{est} - C_i^{gt})^2}, \quad (24)$$

where  $M$  is the number of test images,  $C_i^{gt}$  denotes the exact number of people inside the ROI of the  $i$ -th image and  $C_i^{est}$  is the correspondingly estimated number of people. In the benchmark datasets discussed below, the ROI is the whole image except when explicitly stated otherwise. Note that the number of people can be calculated by summation over the pixels of the ground truth ( $D_i^{gt}$ ) as it is defined in Eq. 9 and the predicted density maps ( $D_i^{est}$ ). We follow the [21] methodology to prepare ground truth density data.

### 4.2 Data Augmentation

We take the benefit of data augmentation to avoid the risk of over-fitting to the small number of training images. We use five types of cropping alongside with a resizing as data augmentations. We crop each image into  $\frac{1}{4}$  of the original dimension. The first four cropped images extract four non-overlapping patches based on each corner of the original image. Furthermore, the fifth crop is randomly cropped from the input scene. For resizing, we just resize the input image to the dimension of (768, 1024) or (1024, 768) depending on the scale of the input data. If height of the input image is bigger than the width of it, we just select (1024, 768), and in other case we resize it to (768, 1024) size.

TABLE 1  
Comparison of the MAE and MSE results obtained with our proposed PDANet and the-state-of-the-art crowd counting approaches on the ShanghaiTech Part A Dataset [25]

Methods	MAE	MSE
ACSCP [39]	75.7	102.7
D-ConvNet-v1 [9]	73.5	112.3
IG-CNN [26]	72.5	118.2
GWTA-CCNN [13]	154	229
DRSAN [40]	69.3	96.4
ic-CNN [41]	68.5	116.2
CSRNet [20]	68.2	115.0
SANet [21]	67.0	104.5
DENet [6]	65.5	101.2
SFCN [42]	64.8	107.5
TEDnet [43]	64.2	109.1
ADCrowdNet [18]	63.2	98.9
PACNN+CSRNet [29]	62.4	102.0
CAN [1]	62.3	100.0
HA-CCN [38]	62.9	94.9
SPN [11]	61.7	99.5
<b>PDANet</b>	<b>60.8</b>	<b>93.4</b>

### 4.3 Experimental Results on the ShanghaiTech Dataset

The ShanghaiTech dataset [25] is one of the most popular and large-scale crowd counting datasets, and it contains 1,198 annotated images with a total of 330,165 people. It contains two parts, *i.e.*, Part A (ShanghaiTech-A) with 482 images randomly collected from the Internet, and Part B (ShanghaiTech-B), including 716 images taken from the urban areas in Shanghai. Each part is divided into two subsets for training and testing. As the challenge caused by diversity of scenarios and variation of congestion differs, it is difficult to estimate the number of pedestrians precisely.

Following [21] and as mentioned in Section 4.1, for setting  $\sigma$  for Part A, we use the KNN method to calculate the average distance between each head and its three nearest heads and  $\beta$  is set to 0.3. For Part B, we set a fixed value 15 for  $\sigma$ . We compare our method with state-of-the-art methods recently published on this dataset.

The quantitative results for ShanghaiTech-A are listed in Table 1. We collect results of the state-of-the-art approaches from their original published papers. It can be seen that our PDANet has achieved an MAE of 60.8 and an MSE of 93.4 in the experiment. Our proposed method also exhibits significant advantages over many top ranked methods such as CSRNet [20], SANet [21], ADCrowdNet [18], HA\_CNN [38], and SPN [11].

Table 2 illustrates the results of our PDANet obtained on the ShanghaiTech-B dataset, which is less crowded than ShanghaiTech-A. The experimental results show that our method outperforms the state-of-the-art approaches. On this dataset, our proposed PDANet has achieved an MAE of 7.1 and an MSE of 10.9, both are better than those of the state-of-the-art results.

These results suggest that our proposed PDANet is able to cope with sparse and dense scenes, thanks to the combination of the pyramid module as mentioned in Sect. 3.3 and the two-branch DAD as described in Sect. 3.5. Because of these, our proposed model can distinguish the crowd level

TABLE 2

Comparison of the MAE and MSE results obtained with our proposed PDANet and the-state-of-the-art crowd counting approaches on the ShanghaiTech Part B dataset [25]

Methods	MAE	MSE
ACSCP [39]	17.2	27.4
D-ConvNet-v1 [9]	18.7	26.0
IG-CNN [26]	13.6	21.1
DecideNet [44]	21.53	31.98
DRSAN [40]	11.1	18.2
ic-CNN [41]	10.7	16.0
CSRNet [20]	10.6	16.0
SANet [21]	8.4	13.6
DENet [6]	9.6	15.4
SFCN [42]	7.6	13.0
TEDnet [43]	8.2	12.8
ADCrowdNet [18]	7.7	12.9
PACNN [29]	8.9	13.5
CAN [1]	7.8	12.2
HA-CCN [38]	8.1	13.4
SPN [11]	9.4	14.4
<b>PDANet</b>	<b>7.1</b>	<b>10.9</b>

of the input scene and analyze the crowd accordingly for better estimation.

#### 4.4 Experimental Results on the WorldExpo10 Dataset

The WorldExpo10 dataset [45] is another large-scale crowd counting benchmark dataset. During the Shanghai WorldExpo 2010, 1,132 video clips were captured by 108 surveillance cameras to produce this large dataset. We follow the standard procedures [45] and take 3,380 annotated images from 103 scenes as the training set and the other remaining frames (600 images) from remaining scenes as testing sets. We prune the crowd density map of the last layer within the Regions of Interest (RoI) in training and testing time.

Table 3 summarizes the prediction results of our PDANet compared with twenty state-of-the-art methods. This table provides MAE results based on five different scenes. The best-performing state-of-the-art methods are CAN [1], ADCrowdNet [18], and PACNN [29] with an average MAE less than 8. However, as shown in the table, our proposed PDANet has achieved an average MAE of 6.0, which suppresses the-state-of-the-art results with a margin of 1.4 over the result achieved by CAN [1]. Furthermore, our PDANet yields the lowest MAE of 4 out of all 5 scenes with an MAE equal to (9.1, 7.3, and 2.2), respectively. As it is demonstrated, the overall performance of our PDANet across various scenes is superior compared with the-state-of-the-art approaches.

#### 4.5 Experimental Results on the UCF Dataset

The UCF CC 50 [46] is one of the most challenging data sets in crowd counting research area due to its limited number of training images and significant variation in the number of people within the datasets (from 94 to 4,543 across images). There is a standard procedure for using this small dataset for training and testing, which is 5-fold cross-validation [46] for training and evaluating models. We choose the setting

TABLE 3

Comparison of the MAE results obtained with our proposed PDANet and the-state-of-the-art crowd counting approaches on the WorldExpo10 dataset [45]

Methods	Sce.1	Sce.2	Sce.3	Sce.4	Sce.5	AVG
ACSCP [39]	2.8	14.05	9.6	8.1	2.9	7.5
D-ConvNet-v1 [9]	1.9	12.1	20.7	8.3	2.6	9.1
IG-CNN [26]	2.6	16.1	10.15	20.2	7.6	11.3
CP-CNN [27]	2.9	14.7	10.5	10.4	5.8	8.86
DRSAN [40]	2.6	11.8	10.3	10.4	3.7	7.76
ic-CNN [41]	17.0	12.3	9.2	8.1	4.7	10.3
CSRNet [20]	2.9	11.5	8.6	16.6	3.4	8.6
SANet [21]	2.6	13.2	9.0	13.3	3.0	8.2
DENet [6]	2.8	10.7	8.6	15.2	3.5	8.2
DecideNet [44]	2.0	13.14	8.9	17.4	4.75	9.23
TEDnet [43]	2.3	10.1	11.3	13.8	2.6	8.0
ADCrowdNet [18]	1.7	14.4	11.5	7.9	3.0	7.7
PACNN [29]	2.3	12.5	9.1	11.2	3.8	7.8
CAN [1]	2.9	12.0	10.0	7.9	4.3	7.4
BSAD [12]	4.1	21.7	11.9	11.0	3.5	10.5
SaCNN [24]	2.6	13.5	10.6	12.5	3.3	8.5
<b>PDANet</b>	<b>1.8</b>	<b>9.1</b>	<b>9.6</b>	<b>7.3</b>	<b>2.2</b>	<b>6.0</b>

TABLE 4

Comparison of the MAE and MSE results obtained with our proposed PDANet and state-of-the-art crowd counting approaches on the UCF crowdcounting dataset [46]

Methods	MAE	MSE
A-CCNN [10]	367.3	423.7
ACSCP [39]	291.0	404.6
D-ConvNet-v1 [9]	288.4	404.7
IG-CNN [26]	291.4	349.4
ASD [19]	196.2	270.9
DRSAN [40]	219.2	250.2
ic-CNN [41]	260.9	365.5
CSRNet [20]	266.1	397.5
SANet [21]	258.4	334.9
DENet [6]	241.9	345.4
SFCN [42]	214.2	318.2
TEDnet [48]	249.4	354.5
ADCrowdNet [18]	257.1	363.5
PACNN [29]	267.9	357.8
CAN [1]	212.2	243.7
HA-CCN [38]	256.2	348.4
SPN [11]	259.2	335.9
SPN+L2SM [47]	188.4	315.3
<b>PDANet</b>	<b>119.8</b>	<b>159</b>

similar to the ShanghaiTech-A [25] setting for generating ground truth density maps.

We present the results achieved on this dataset in Table 4. It is shown in this table that our PDANet outperforms the state-of-the-art models by a significant margin. We achieve an MAE of 136.6 with an MSE of 198.4, which is about 28 percent better than SPN+L2SM [47], the best-performing benchmark model. In our experiments, we observe that our PDANet is able to estimate the number of people accurately in all subsets. We will explore the results in details in the Ablation study section.

Overall, it can be concluded that our proposed PDANet can work well on both sparse and dense scenarios.

TABLE 5

Comparison of the MAE and MSE results obtained with our proposed PDANet and the-state-of-the-art crowd counting approaches on the UCSD crowd-counting dataset [49]

Methods	MAE	MSE
Density Learning [5]	1.70	1.28
Learning to Count [43]	1.70	2.16
Count Forest [50]	1.43	1.30
Arteta et al. [51]	<b>1.24</b>	1.31
Zhang et al. [45]	1.70	1.2
Switch-CNN [12]	1.62	2.10
ConvLSTM [52]	1.30	1.79
A-CCNN [10]	1.51	1.36
Bidirectional ConvLSTM [52]	1.13	1.43
CSRNet [20]	1.16	1.47
ACSCP [39]	1.04	1.35
SANet [21]	1.02	1.29
BSAD [53]	1.00	1.40
SPN [11]	1.03	1.32
ADCrowdNet(DME) [18]	0.98	1.25
PACNN [29]	<b>0.89</b>	<b>1.18</b>
<b>PDANet</b>	0.93	1.21

#### 4.6 Experimental Results on the UCSD Dataset

The UCSD dataset [49] is the dataset that we conduct experiments on. This dataset contains 2,000 annotated frames, which are captured by a CCTV camera from pedestrians on a walkway. This dataset comes with ROIs, and most of the existing crowd counting approaches have reported the results based on ROIs. In the experiment, we used Frames 601 through 1400 for training and the remaining out of 2000 for testing. Table 5 shows the MAE and MSE results obtained on this dataset in comparison with other state-of-the-art approaches. By comparing with the 16 approaches, it is shown that our PDANet is the second-best on this dataset with an MAE of .93 and an MSE=1.21, which is very close to the PACNN [29] results on UCSD dataset.

### 5 ABLATION STUDY

To further demonstrate the effectiveness of each component proposed in our PDANet model, we conduct series of ablation studies.

In this section, we first visualize some examples of the results achieved, and then explore some of our model components and discuss their outputs to analyze the effectiveness of each component. The ablation studies are conducted on the UCF CC50 [46] and ShanghaiTech [25] datasets.

#### 5.1 Density Map Visualization

Qualitatively, we visualize the density maps generated by our proposed PDANet method on the ShanghaiTech Part A, Part B [25], and UCF CC 50 [46] datasets in comparison with the original ground truth (GT). These are shown in Figs. 7, 8 and 9. In these figures, three sample images corresponding to low, medium and high density scenes are selected from each dataset. For each sample image, we show the input image with an index of 0, and its Ground Truth (GT) density map, its estimated overall density map, its estimated dense and sparse density maps with an index of 1 to 4, respectively.

Fig. 7 presents examples of results obtained on the ShanghaiTech Part A dataset. For this dataset, we select three images with a total crowd count of 99, 582, and 2270 respectively, representing input scenes of low (top row of Fig. 7), medium (middle row of Fig. 7) and high (bottom row of Fig. 7) crowdedness scenes.

As shown in this figure, the estimated counts and the actual ground truth counts are very close to each other, demonstrating that our proposed model performs well in the scenes of various crowdedness levels. For instance, for the image in the bottom row of Fig. 7, the ground truth count is 2270, while our prediction is 2213, which is a reasonable estimation for such a highly crowded input scene. On the other hand, for low crowdedness scenes, such as Fig. 7(a0), our proposed PDANet also produces accurate density maps. Fig. 7 also shows that our proposed model can accurately discriminate more crowded areas from less crowded ones. When looking further into the results of dense and sparse scenes, we can draw a conclusion that our model works well for extracting better information for more accurate overall density map estimation.

Fig. 8 presents results on three sample scenes from the ShanghaiTech Part B dataset. In this figure, we choose three sample images with crowd counts varying from 29 to 251, corresponding to low, medium, and high crowdedness images. These figures also demonstrate that our PDANet works well in low crowdedness areas. For instance, in sub-figure Fig. 8(a0), the predicted density maps and the actual density maps appear to be very similar, and so are the estimated count and the ground truth counts of crowd in the scene. Fig. 8 also shows that for medium and low crowdedness scenes, our proposed model produces accurate density maps.

Fig. 9 illustrates results on three sample images from the UCF CC 50 dataset [46], which is a highly crowded challenging dataset. In this figure, we choose three images with crowd counts equal to 555, 1852, and 4706, corresponding to low, medium, and high crowdedness scenes, respectively. We can see that our proposed PDANet works well in highly crowded images as well as low and mid crowdedness images. It is also evident that our proposed DAD model helps to localize dense and non-dense areas of the input image. However, in crowded medium crowdedness images, it is evident that some plant areas are considered as crowd, due to the nature of the grayscale input image.

#### 5.2 Effectiveness of the PFE Module

In the first experiment, we investigate the impact of different numbers of GAP modules on the baseline model (baselineAD, *i.e.*, a PDANet without the PFE module).

We test our proposed model with different numbers of GAPs from 0 GAP (baselineAD) to 10 GAPs. We obtain the GAPs of input feature maps by resizing them with divisors of 2, 4, 8, 3, 6, 10, 5, 7, and 9, respectively. For example, for the input feature map with size of  $H \times W$ , we apply GAP with divisor of 2 to generate the corresponding GAPs' feature maps with the size of  $\frac{H}{2} \times \frac{W}{2}$ . We sort these numbers with the order of use. For example, if we aim to utilize 3 GAPs, we divide the input feature maps with the divisors of 2, 4, ..., respectively, to capture the information of various scales from the input feature maps.

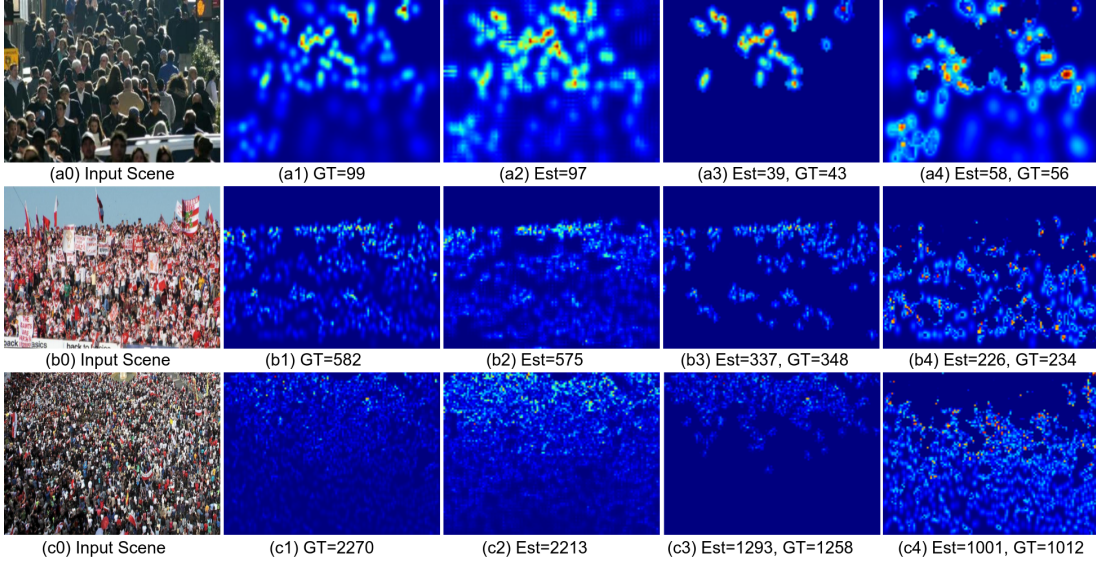


Fig. 7. Results of the estimated density maps of images from the ShanghaiTech Part A dataset. We illustrate three test images (a0, b0, c0), their actual ground truth (a1, b1, c1), our estimated overall density maps (a2, b2, c2), our estimated density maps for dense areas (a3, b3, c3), and our estimated density maps for sparse areas and their crowd counts (a4, b4, c4).

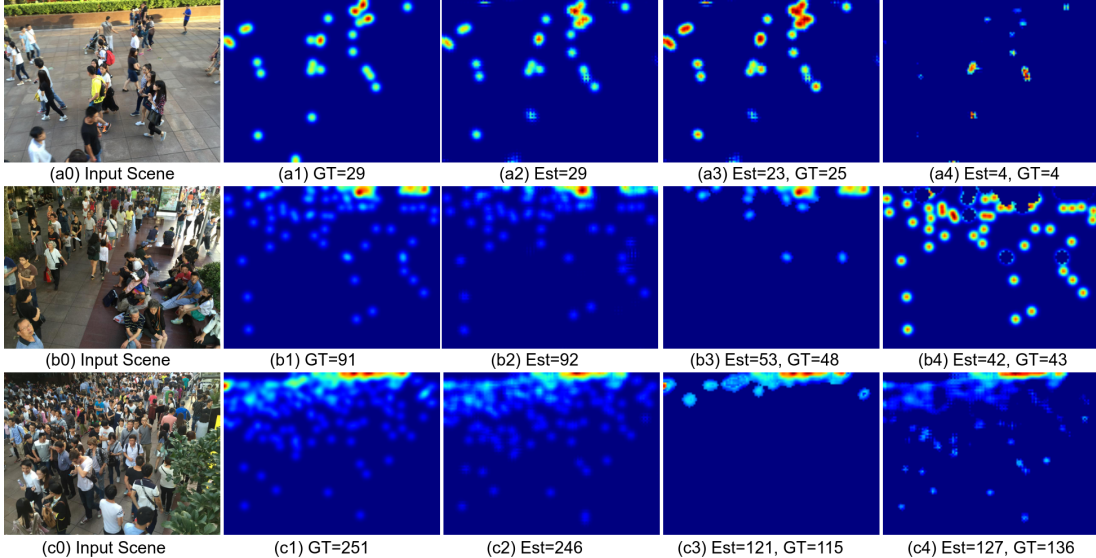


Fig. 8. Results of the estimated density maps of images from the ShanghaiTech Part B dataset. We illustrate three test images (a0, b0, c0), their actual ground truth (a1, b1, c1), our estimated overall density maps (a2, b2, c2), our estimated density maps for dense areas (a3, b3, c3), and our estimated density maps for sparse areas and their crowd counts (a4, b4, c4).

Fig. 10 presents the results of this experiment on Part0 of the UCF CC 50 dataset. In this figure, we report the achieved MAE and MSE results for the PFE module with various GAPs. As shown in this graph, our PDANet has achieved an MAE of 157 and an MSE of 202 at three GAP settings (the third one in Fig. 10), utilizing the division factors 2, 4, and 8, as three different scales of input feature maps. As it is shown, it outperforms other PDANets with more or fewer GAPs modules, as well as the baselineAD model. Among the various PFE modules, PFEs with three GAPs and six GAPs provide better crowd level predictions in Part0. Fig. 10 also shows that the PDANet with GAPs in the worst-case still improves the estimation of the baselineAD (MAE of 202 vs. 300).

We have tested the effect of different numbers of pyramid GAPs on the ShanghaiTech dataset as well. The test results are shown in Fig. 11 and Fig. 12. The results again show that our proposed PDANet (with three GAPs) outperforms the baselineAD and other PDANet models with more or fewer GAPs. The results of the other numbers of GAPs fluctuate slightly from an MAE of 61 to 94 for Part A and an MAE of 7.3 to 11.9 for Part B, which are very consistent. In summary, the PFE with three GAPs works better in the PDANet model for crowd counting. We believe that by using scale like the one used in PDANet (three GAPs), the output feature maps have more accurate scale information than that of the other PDANet models with different numbers of GAPs. On the other hand, increasing

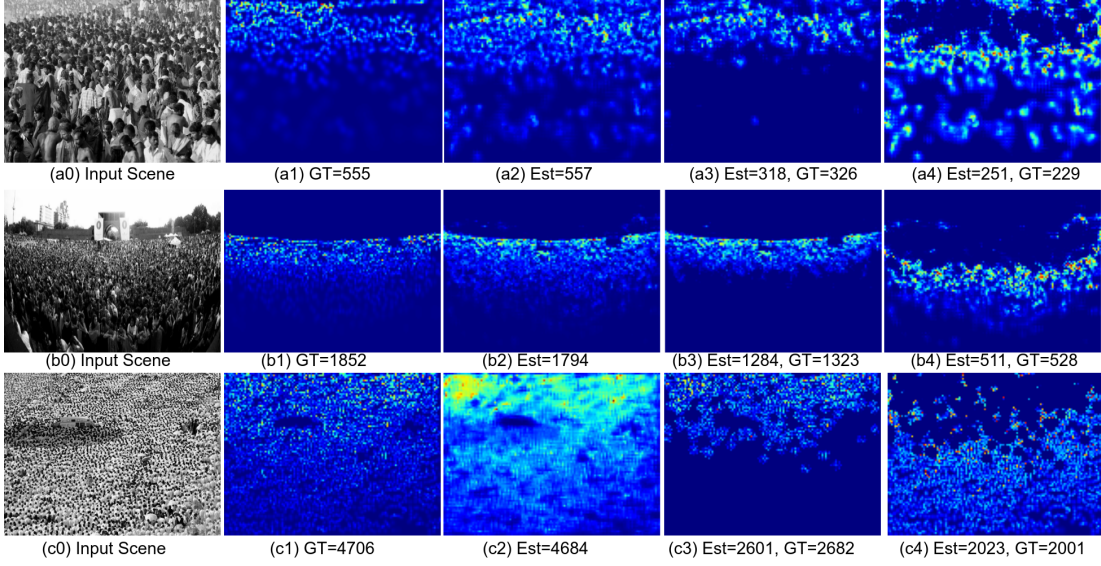


Fig. 9. Results of the estimated density maps of images from the UCF CC 50 dataset [46]. We present three test images (a0, b0, c0), their actual ground truth (a1, b1, c1), our estimated overall density maps (a2, b2, c2), our estimated density maps for dense areas (a3, b3, c3), and our estimated density maps for sparse areas and their crowd counts (a4, b4, c4).

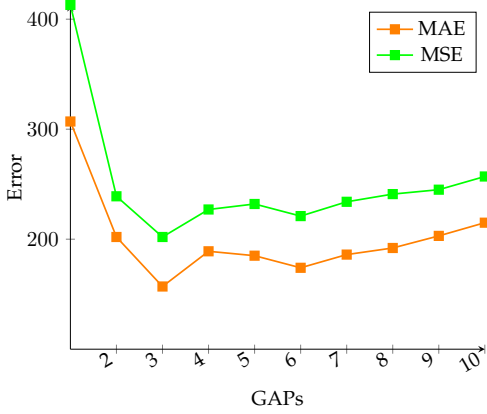


Fig. 10. Comparison of MAE and MSE results between various numbers of GAP layers on Part 0 of the UCF crowd counting dataset [46]

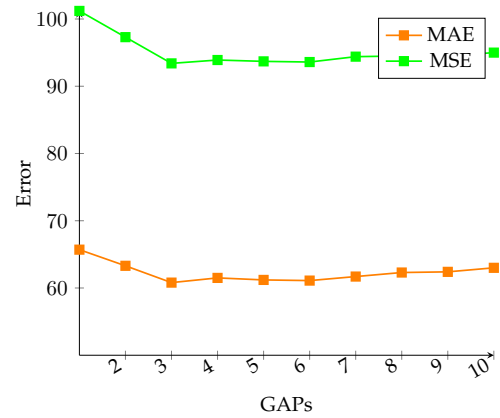


Fig. 11. Comparison of the MAE and MSE results between various numbers of GAP layers on the ShanghaiTech PartA dataset [25]

the number of GAPs will increase the number of parameters, which in turn increases the complexity of the model. Thus, the performance of the model will slightly decrease with the rise of over-fitting issues. Overall, our proposed PDANet (3GAP) has the most optimal number of parameters for the PFE modules, too. Thus, it can be trained more efficiently by the model to capture the essential scale information.

### 5.3 Effectiveness of the Attention Module

To gain an insight into the effectiveness of the Attention Module, we perform an ablation study to demonstrate the contribution of the module to the performance of the proposed model. We compare the performance of our design choices with the baseline with PFE and DAD module. Tables 6 and 7 illustrate the results obtained on UCF CC 50 and ShanghaiTech dataset. Part0 of UCF CC 50 dataset has the greatest improvement in terms of MAE/MSE, but the improvement on the performance of part1 to part4 is

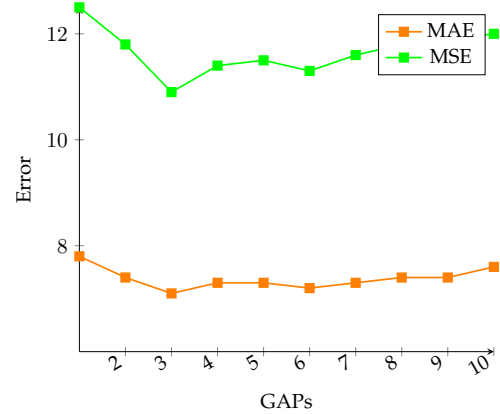


Fig. 12. Comparison of MAE and MSE results between various numbers of GAP layers on the ShanghaiTech PartB dataset [25]

TABLE 6

Effect of adopting the attention module on crowd counting performance based on the UCF crowd-counting dataset [46]

UCF CC 50						
Metrics	Part0	Part1	Part2	Part3	Part4	AVG
BaselinePD	MAE	205	132	86	127	112
	MSE	243	164	111	188	131
PDANet	MAE	157	128	80	126	108
	MSE	202	182	95	186	130

TABLE 7

Effect of Attention Module on crowd counting performance based on the ShanghaiTech crowd-counting dataset [25]

Metrics	ShanghaiTech	
	PartA	PartB
BaselinePD	MAE	62.3
	MSE	98.6
PDANet	MAE	60.8
	MSE	93.4

small. As shown in Table 7, we have achieved more or less the same improvement in crowd counting by adopting the attention module.

Overall, we use the attention module for localizing the crowd area and improving the performance of our model. As shown in these tables, we have achieved our goal by combining spatial/channel based attention, which is based on sparse and dense crowded areas. Thus, these results prove the application of the attention module on improving the accuracy of the crowd counting model.

#### 5.4 Effectiveness of the Classification and DAD Modules

To address the density variation within and between different input images, we have proposed a two-branch DAD module. In this section, we aim to understand the effect of this module in our overall performance improvement. Same as in previous sections, we compare the results of our PDANet with DAD and without DAD (passing the data to one branch only) on both UCF CC 50 and the ShanghaiTech datasets.

Tables 8 and 9 show the experimental results obtained on the UCF and ShanghaiTech datasets, respectively. As seen from Table 8, we are able to boost the accuracy of crowd counting by around 20 percent for the UCF dataset in all subsets. With the ShanghaiTech dataset, we have also achieved a noticeable improvement in accuracy with the help of the DAD module.

These results demonstrate the effectiveness of our initial idea about processing the sparse and dense crowded feature maps separately. We believe that the DAD module helps the PDANet generate proper density maps for both high and low crowdedness areas in the images, and simultaneously, it guides the proposed model to react to the difference of the input images with different crowdedness.

TABLE 8

Effect of classification and DAD modules on crowd counting performance based on the UCF crowd counting dataset [46]

UCF CC50						
Metrics	Part0	Part1	Part2	Part3	Part4	AVG
BaselinePA	MAE	217	151	116	146	114
	MSE	267	183	124	185	138
PDANet	MAE	157	128	80	126	108
	MSE	202	182	95	186	130

TABLE 9

Effectiveness of the classification and DAD modules on crowd counting performance based on the ShanghaiTech crowd-counting dataset [25]

Metrics	Shanghai	
	PartA	PartB
BaselinePA	MAE	66.5
	MSE	104.1
PDANet	MAE	60.8
	MSE	93.4

## 6 CONCLUSION

In this work, we have introduced a novel deep architecture called Pyramid Density-Aware Attention-based network (PDANet) for crowd counting. The PDANet incorporated pyramid features and attention modules with a density-aware decoder to address the huge density variation within the crowded scenes. The proposed PDANet has utilized a classification module for passing the pyramid features to the most suitable decoder branch to provide more accurate crowd counting with two-scale density maps. To aggregate these density maps, we have taken the benefit of the sigmoid function and produced a gating mask for producing the final density map. Extensive experiments on various benchmark datasets have demonstrated the performance of our PDANet in terms of robustness, accuracy, and generalization. Our approach is able to achieve superior performance compared with the state-of-the-art results on three challenging crowd counting datasets (ShanghaiTech, UCF CC 50 and World Expo 10), especially in UCF 50 with more than 25 immediate improvements in the results based on all evaluation metrics.

## REFERENCES

- W. Liu, M. Salzmann, and P. Fua, "Context-aware crowd counting," in *CVPR*, 2019, pp. 5099–5108.
- J. Shao, K. Kang, C. Change Loy, and X. Wang, "Deeply learned attributes for crowded scene understanding," in *CVPR*, 2015, pp. 4657–4666.
- B. Zhou, X. Wang, and X. Tang, "Understanding collective crowd behaviors: Learning a mixture model of dynamic pedestrian-agents," in *CVPR*. IEEE, 2012, pp. 2871–2878.
- A. B. Chan and N. Vasconcelos, "Bayesian poisson regression for crowd counting," in *ICCV*. IEEE, 2009, pp. 545–551.
- V. Lempitsky and A. Zisserman, "Learning to count objects in images," in *NIPS*, 2010, pp. 1324–1332.
- L. Liu, J. Jiang, W. Jia, S. Amirgholipour, M. Zeibots, and X. He, "Denet: A universal network for counting crowd with varying densities and scales," *arXiv*, 2019.
- H. Li, X. He, H. Wu, S. A. Kasmani, R. Wang, X. Luo, and L. Lin, "Structured inhomogeneous density map learning for crowd counting," *arXiv*, 2018.

[8] L. Liu, S. Amirgholipour, J. Jiang, W. Jia, M. Zeibots, and X. He, "Performance-enhancing network pruning for crowd counting," *Neurocomputing*, 2019.

[9] L. Zhang, Z. Shi, M.-M. Cheng, Y. Liu, J.-W. Bian, J. T. Zhou, G. Zheng, and Z. Zeng, "Nonlinear regression via deep negative correlation learning," *TPAMI*, 2019.

[10] S. Amirgholipour, X. He, W. Jia, D. Wang, and M. Zeibots, "Accnn: Adaptive ccnn for density estimation and crowd counting," in *ICIP*. IEEE, 2018, pp. 948–952.

[11] X. Chen, Y. Bin, N. Sang, and C. Gao, "Scale pyramid network for crowd counting," in *WACV*, Jan 2019, pp. 1941–1950.

[12] D. Sam, S. Surya, and R. Babu, "Switching convolutional neural network for crowd counting," in *CVPR*, vol. 1/3, 2017, p. 6.

[13] D. B. Sam, N. N. Sajjan, H. Maurya, and R. V. Babu, "Almost unsupervised learning for dense crowd counting," in *AAAI*, vol. 27, 2019.

[14] K. Simonyan and A. Zisserman, "Very deep convolutional networks for large-scale image recognition," *arXiv*, 2014.

[15] C. Szegedy, W. Liu, Y. Jia, P. Sermanet, S. Reed, D. Anguelov, D. Erhan, V. Vanhoucke, and A. Rabinovich, "Going deeper with convolutions," in *CVPR*, 2015, pp. 1–9.

[16] C. Szegedy, V. Vanhoucke, S. Ioffe, J. Shlens, and Z. Wojna, "Rethinking the inception architecture for computer vision," in *CVPR*, 2016, pp. 2818–2826.

[17] D. Kang and A. Chan, "Crowd counting by adaptively fusing predictions from an image pyramid," *arXiv*, 2018.

[18] N. Liu, Y. Long, C. Zou, Q. Niu, L. Pan, and H. Wu, "Adcrowdnet: An attention-injective deformable convolutional network for crowd understanding," in *CVPR*, 2019, pp. 3225–3234.

[19] X. Wu, Y. Zheng, H. Ye, W. Hu, J. Yang, and L. He, "Adaptive scenario discovery for crowd counting," in *ICASSP*. IEEE, 2019, pp. 2382–2386.

[20] Y. Li, X. Zhang, and D. Chen, "Csrnet: Dilated convolutional neural networks for understanding the highly congested scenes," in *CVPR*, 2018, pp. 1091–1100.

[21] X. Cao, Z. Wang, Y. Zhao, and F. Su, "Scale aggregation network for accurate and efficient crowd counting," in *ECCV*, 2018, pp. 734–750.

[22] K. Kang and X. Wang, "Fully convolutional neural networks for crowd segmentation," *arXiv*, 2014.

[23] X. Chen, Y. Bin, N. Sang, and C. Gao, "Scale pyramid network for crowd counting," in *WACV*. IEEE, 2019, pp. 1941–1950.

[24] D. Onoro-Rubio and R. Lpez-Sastre, "Towards perspective-free object counting with deep learning," in *ECCV*. Springer, 2016, pp. 615–629.

[25] Y. Zhang, D. Zhou, S. Chen, S. Gao, and Y. Ma, "Single-image crowd counting via multi-column convolutional neural network," in *CVPR*, 2016, pp. 589–597.

[26] D. Babu Sam, N. N. Sajjan, R. Venkatesh Babu, and M. Srinivasan, "Divide and grow: Capturing huge diversity in crowd images with incrementally growing cnn," in *CVPR*, 2018, pp. 3618–3626.

[27] V. A. Sindagi and V. M. Patel, "Generating high-quality crowd density maps using contextual pyramid cnns," in *ICCV*. IEEE, 2017, pp. 1879–1888.

[28] D. Deb and J. Ventura, "An aggregated multicolunm dilated convolution network for perspective-free counting," in *CVPR Workshops*, 2018, pp. 195–204.

[29] M. Shi, Z. Yang, C. Xu, and Q. Chen, "Revisiting perspective information for efficient crowd counting," in *CVPR*, 2019, pp. 7279–7288.

[30] J. Wan, W. Luo, B. Wu, A. B. Chan, and W. Liu, "Residual regression with semantic prior for crowd counting," in *CVPR*, 2019, pp. 4036–4045.

[31] R. R. Varior, B. Shuai, J. Tighe, and D. Modolo, "Scale-aware attention network for crowd counting," *arXiv*, 2019.

[32] H. Zhao, J. Shi, X. Qi, X. Wang, and J. Jia, "Pyramid scene parsing network," in *CVPR*, 2017, pp. 2881–2890.

[33] J. Hu, L. Shen, and G. Sun, "Squeeze-and-excitation networks," in *CVPR*, 2018, pp. 7132–7141.

[34] A. G. Roy, N. Navab, and C. Wachinger, "Concurrent spatial and channel squeeze & excitationin fully convolutional networks," in *MICCAI*. Springer, 2018, pp. 421–429.

[35] S. Jetley, N. A. Lord, N. Lee, and P. H. Torr, "Learn to pay attention," *arXiv*, 2018.

[36] J. Schlemper, O. Oktay, L. Chen, J. Matthew, C. Knight, B. Kainz, B. Glocker, and D. Rueckert, "Attention-gated networks for improving ultrasound scan plane detection," *arXiv*, 2018.

[37] S. Zagoruyko and N. Komodakis, "Paying more attention to attention: Improving the performance of convolutional neural networks via attention transfer," *arXiv*, 2016.

[38] V. A. Sindagi and V. M. Patel, "Ha-ccn: Hierarchical attention-based crowd counting network," *TIP*, 2019.

[39] Z. Shen, Y. Xu, B. Ni, M. Wang, J. Hu, and X. Yang, "Crowd counting via adversarial cross-scale consistency pursuit," in *CVPR*, 2018, pp. 5245–5254.

[40] L. Liu, H. Wang, G. Li, W. Ouyang, and L. Lin, "Crowd counting using deep recurrent spatial-aware network," *arXiv*, 2018.

[41] V. Ranjan, H. Le, and M. Hoai, "Iterative crowd counting," in *Proceedings of the European Conference on Computer Vision (ECCV)*, 2018, pp. 270–285.

[42] Q. Wang, J. Gao, W. Lin, and Y. Yuan, "Learning from synthetic data for crowd counting in the wild," in *CVPR*, 2019, pp. 8198–8207.

[43] L. Fiaschi, U. Kóthe, R. Nair, and F. Hamprecht, "Learning to count with regression forest and structured labels," in *ICPR*, vol. 21. IEEE, 2012, pp. 2685–2688.

[44] J. Liu, C. Gao, D. Meng, and A. G. Hauptmann, "Decidernet: Counting varying density crowds through attention guided detection and density estimation," in *CVPR*, 2018, pp. 5197–5206.

[45] C. Zhang, H. Li, X. Wang, and X. Yang, "Cross-scene crowd counting via deep convolutional neural networks," in *CVPR*, 2015, pp. 833–841.

[46] H. Idrees, I. Saleemi, C. Seibert, and M. Shah, "Multi-source multi-scale counting in extremely dense crowd images," in *CVPR*, 2013, pp. 2547–2554.

[47] C. Xu, K. Qiu, J. Fu, S. Bai, Y. Xu, and X. Bai, "Learn to scale: Generating multipolar normalized density map for crowd counting," *arXiv*, 2019.

[48] X. Jiang, Z. Xiao, B. Zhang, X. Zhen, X. Cao, D. Doermann, and L. Shao, "Crowd counting and density estimation by trellis encoder-decoder networks," in *CVPR*, 2019, pp. 6133–6142.

[49] A. Chan, Z. Liang, and N. Vasconcelos, "Privacy preserving crowd monitoring: Counting people without people models or tracking," in *CVPR*. IEEE, 2008, pp. 1–7.

[50] V. Pham, T. Kozakaya, O. Yamaguchi, and R. Okada, "Count forest: Co-voting uncertain number of targets using random forest for crowd density estimation," in *ICCV*, 2015, pp. 3253–3261.

[51] C. Arteta, V. Lempitsky, J. Noble, and A. Zisserman, "Interactive object counting," in *ECCV*. Springer, 2014, pp. 504–518.

[52] F. Xiong, X. Shi, and D.-Y. Yeung, "Spatiotemporal modeling for crowd counting in videos," in *ICCV*, 2017, pp. 5151–5159.

[53] S. Huang, X. Li, Z. Zhang, F. Wu, S. Gao, R. Ji, and J. Han, "Body structure aware deep crowd counting," *TIP*, vol. 27, no. 3, pp. 1049–1059, 2017.